CMES, vol.3, no.1, pp.103-116, 2002

Nodal Constraint, Shear Deformation and Continuity Effects Related to the Modeling of Debonding of Laminates, Using Plate Elements

E.H. Glaessgen[1], **W.T. Riddell**[2], **and I.S. Raju**[1]

Abstract: The effects of several critical assumptions and parameters on the computation of strain energy release rates for delamination and debond configurations modeled with plate elements have been quantified. The method of calculation is based on the virtual crack closure technique (VCCT), and models of the upper and lower surface of the delamination or debond that use two-dimensional (2D) plate elements rather than three-dimensional (3D) solid elements. The major advantages of the plate element modeling technique are a smaller model size and simpler configurational modeling. Specific issues that are discussed include: constraint of translational degrees of freedom, rotational degrees of freedom or both in the neighborhood of the debond front; shear deformation assumptions; and continuity of material properties and section stiffness in the vicinity of the debond front. Where appropriate, the plate element analyses are compared with corresponding two-dimensional plane strain analyses.

1 Introduction

Skin-stiffener debonding is considered a critical failure mode for stiffened composite panels. Figure 1 shows the elements of a composite skin-stiffened panel including the skin and stiffeners. Simplified configurations that can be used to study the details of the skin-stiffener debonding are shown in Figures 1(b) and 1(c). Much of the research on skin-stiffener debonding failure has focused on the calculation of skin-stiffener interface stresses [Wang and Biggers (1984); Hyer and Cohen (1987); Cohen and Hyer (1988)]. These interface stresses initiate debonds at the edges of the stiffening elements as shown in Figures 1(b) and 1(c). Fracture mechanics approaches utilizing the concept of strain energy release rate have been used to predict the growth of these types of skin-stiffener debonds with considerable success [O'Brien (1982); Wang and Crossman (1980); Whitcomb (1988)]. Recently, Chow and Atluri (1996) presented simple formulae relating stress intensity factors to energy release rates for isotropic, orthotropic and anisotropic bimaterial continua. Their work presents an innovative approach to solving the perennial problem of the bimaterial interface crack. A related evaluation of energy release rates in buckled delaminations was given by Naganarayana and Atluri (1995) and a detailed review of analyses for debonding of laminated composites can be found in Atluri (1997). While primarily the finite element methods were used in these works, recent literature shows the use of other methods such as the boundary element method for fracture mechanics analysis for anisotropic plates [Shiah and Tan (2000)].

Models based on quasi-3D (extruded 2D) or 3D brick finite elements have been used to study edge delamination and near-surface delamination of composites [O'Brien (1982); Wang and Crossman (1980); Whitcomb (1988)]. Since many layers of brick elements through-the-thickness are often required to model both the skin panel and the associated stiffeners, the size of finite element models required for accurate analyses may become prohibitively large. However, finite element analysis using plate elements can be implemented to evaluate strain energy release rates for debonds at the skin-stiffener interface while requiring many fewer degrees of freedom than needed by full 3D analyses [Wang, Raju, and Sleight (1995); Raju, Sistla, and Krishnamurthy (1996); Wang, Raju, Davila, and Sleight (1993); Wang and Raju (1996)]. These plate element models, in conjunction with the virtual crack closure technique (VCCT), can be used to evaluate the values for mode I and mode II strain energy release rates accurately. However, several issues arise pertaining to the techniques of modeling debonding with these elements.

---

[1] NASA Langley Research Center
Hampton, VA 23681
[2] Volpe National Transportation Systems Center
Cambridge, MA 02142

The objective of this paper is to quantify several issues pertaining to the computation of strain energy release rates for delamination and debond configurations modeled with plate elements. The issues and parameters studied are: constraint of translational degrees of freedom, rotational degrees of freedom or both in the neighborhood of the debond front; shear deformation assumptions; and continuity of material properties and section stiffness in the vicinity of the debond. The discussions that are presented in this paper are pertinent to both delamination and debond analyses for metallic and composite skin-stiffener configurations. In this paper, both an isotropic homogeneous skin and stiffener in a symmetric double cantilever beam (DCB) configuration and a composite skin with composite stiffener flanges modeled as homogeneous transversely isotropic materials in a skin-stiffener debond configuration are considered.

2 Analysis

The skin-stiffener debond configuration and the two simplifying cases that are included in this paper are presented in this section. Next, definitions and procedures used in the literature for the calculation of the strain energy release rates are briefly discussed. Finally, modeling issues related to these calculations are presented and discussed.

2.1 Skin-Stiffener Modeling

A typical composite skin-stiffener configuration with blade stiffeners is shown in Figure 1(a). Since the configuration and loading are very complex, simplified configurations are used in these analyses to quantify the effects of the critical assumptions and parameters of interest on the calculation of strain energy release rates. When debonding between the flange and skin takes place along the entire length of the stiffener, a representative portion of the flange and skin can be analyzed as shown in Figures 1(b) and 1(c). The double cantilever beam configuration, shown in Figure 1(b) and in more detail in Figure 2, is a simple configuration in which only mode I loading is assumed. The mixed-mode skin-flange debond configuration, shown in Figure 1(c) and in more detail in Figure 3, has combined mode I and mode II loading. These two configurations are studied in this paper.

The debond configurations are modeled with 2D (plane strain) finite elements (Figure 2(b)) and with non shear-

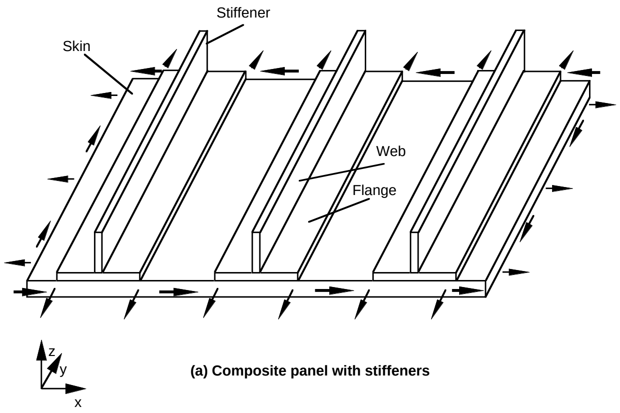

(a) Composite panel with stiffeners

(b) Double cantilever beam **(c) Flange-skin debond**

Figure 1 : Composite Skin-siffened Panel

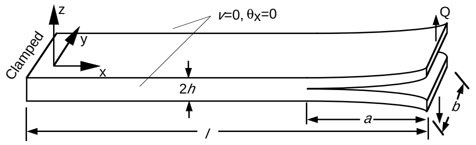

(a) Double cantilever beam configuration

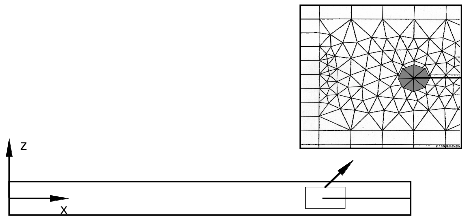

(b) Plane strain model with crack tip detail showing rosette of 6-noded quarter point triangles

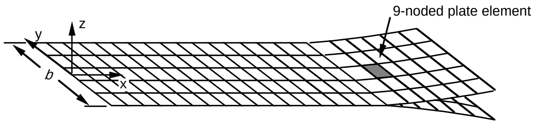

(c) Plate element model - cylindrical bending

Figure 2 : Double cantilever beam configuration and models.

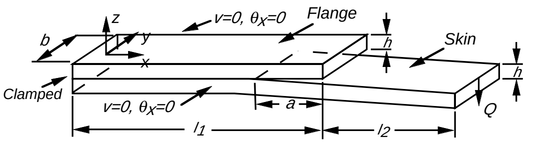

(a) Flange-skin debond configuration

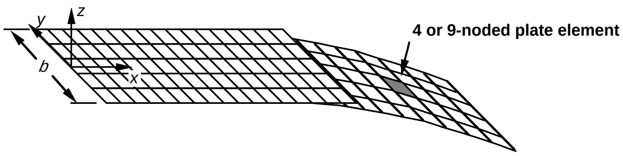

(b) Plate element model - cylindrical bending

Figure 3 : Flange-skin debond configuration and models.

deformable (Figures 2(c) and 3(b)) and first order shear-deformable plate elements (Figure 3(b)). Results from the two-dimensional (plane strain) analyses, which account for shear deformation, will be used as a baseline for comparison with the plate element results. The influence of modeling shear deformation on calculated strain energy release rates is illustrated by comparing results from the plate element models with those from the plane strain analyses.

In all of the plate finite element models considered herein, the skin and the stiffener are modeled as separate, flat plates. Conventional plate modeling inherently assumes that the reference surface of the plate coincides with the middle surface. Thus, the skin and stiffener are usually modeled by plate elements with nodes at their respective mid-planes. This conventional method is not convenient for modeling debonding because it entails complex constraints to tie the stiffener flange nodes to the corresponding skin nodes. A more convenient approach, taken in the present analysis, is to place the skin nodes and the stiffener flange nodes along the interface between the skin and the stiffener. The positioning of these nodes at the interface is performed by defining an offset distance from the mid-plane of both the skin and the stiffener flange (see Wang, Raju, Davila, and Sleight (1993); Wang and Raju (1996)), as shown in Figure 4.

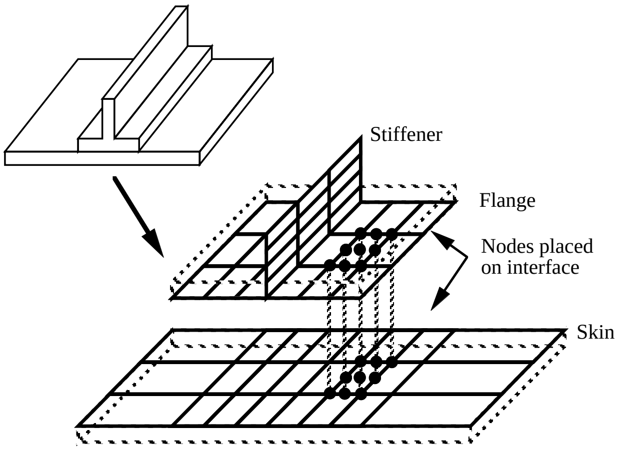

Figure 4 : Plate Element Model of Skin and Stiffener.

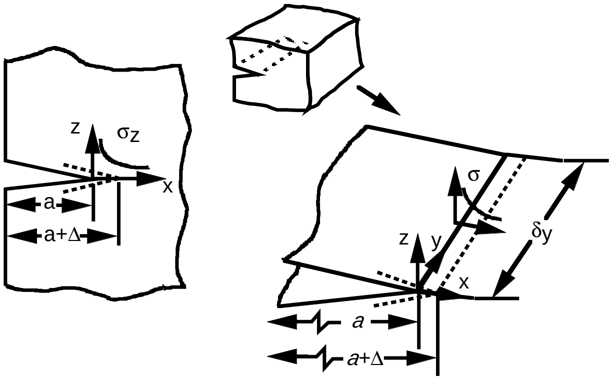

(a) Crack in 2D plate

(b) Through-crack in 3D body

Figure 5 : VCCT approach for G-calculation

2.2 Strain Energy Release Rates

Figure 5 shows an edge debond of length a in a large plate of unit thickness. The strain energy release rate, G, for self-similar debond growth under constant load is defined as [Broek (1987)]

$$G = \frac{\partial W}{\partial A} - \frac{\partial U}{\partial A} \tag{1}$$

where U is the total strain energy of the body, W is the external work done on the body and A is the debond surface area.

2.2.1 2D Analysis

To calculate strain energy release rates, G, from elasticity solutions Irwin proposed the virtual crack closure technique (VCCT) [Irwin (1958)]. Here, G is calculated by considering the work required to close the debond from $a+\Delta$ to a in a 2D plane analysis as shown in Figure 5(a). Energy release rates can be separated into mode I and mode II components and calculated by

$$\begin{aligned}
G_I &= \lim_{\Delta\to 0}\left\{\frac{-1}{2\Delta}\int_0^{\Delta}\sigma_z(x)\,w(\Delta-x)\,dx\right\}\\
G_{II} &= \lim_{\Delta\to 0}\left\{\frac{-1}{2\Delta}\int_0^{\Delta}\sigma_{xz}(x)\,u(\Delta-x)\,dx\right\}\\
G_{Total} &= G_I+G_{II}
\end{aligned}\qquad(2)$$

where w and u are the debond opening and sliding displacements, respectively, and σ_z and σ_{xz} are the normal and shear stresses ahead of the debond front. Discussions of the application of this technique to calculating the strain energy release rates from a single finite element solution using nodal forces ahead of the debond front and the debond opening displacements behind the debond front are given in Rybicki and Kanninen (1977) and Raju (1987).

2.2.2 3D Analysis

The VCCT can also be applied to 3D configurations such as the one shown in Figure 5(b). Here, G can be separated into mode I, mode II and mode III components by

$$\begin{aligned}
G_I &= \lim_{\Delta\to 0}\left\{\frac{-1}{2\Delta\delta y}\int_y^{y+\delta y}\left[\int_0^{\Delta}\sigma_z(x,y,0)\,w(\Delta-x,y,0)\,dx\right]dy\right\}\\
G_{II} &= \lim_{\Delta\to 0}\left\{\frac{-1}{2\Delta\delta y}\int_y^{y+\delta y}\left[\int_0^{\Delta}\sigma_{xz}(x,y,0)\,u(\Delta-x,y,0)dx\right]dy\right\}\\
G_{III} &= \lim_{\Delta\to 0}\left\{\frac{-1}{2\Delta\delta y}\int_y^{y+\delta y}\left[\int_0^{\Delta}\sigma_{xy}(x,y,0)\,v(\Delta-x,y,0)dx\right]dy\right\}\\
G_{Total} &= G_I+G_{II}+G_{III}
\end{aligned}\qquad(3)$$

where w, u and v are the debond face displacements, and σ_z, σ_{xz} and σ_{xy} are the corresponding normal and shear stresses ahead of the debond front. For the purposes of this paper, only mode I and mode II load conditions will be considered to allow comparison with plane strain results.

The VCCT has been implemented in three-dimensional finite element analyses, where the region near the debond front is modeled by either eight or twenty-noded brick elements [Raju, Sistla, and Krishnamurthy (1996)]. As in two-dimensional analysis, the individual mode strain energy release rates can be calculated from the nodal forces and displacements near the debond front obtained from a single finite element analysis.

2.3 Modeling Issues

A method for the calculation of strain energy release rates for debond problems using plate elements is presented in Wang, Raju, Davila, and Sleight (1993) and Wang and Raju (1996). In this method of modeling debonding with plate elements, several critical assumptions are made regarding the effects of:

- constraint of translational degrees of freedom, rotational degrees of freedom or both in the neighborhood of the debond front,
- shear deformation assumptions, and
- continuity of material properties and section stiffness in the vicinity of the debond front

on the values of strain energy release rate computed using the virtual crack closure technique. The effects of each of these assumptions on the response of isotropic double cantilever beam and composite orthotropic debond configurations are discussed in detail in the results section of this paper.

2.3.1 Nodal Constraint

Compatibility conditions require that the translations at $z=0^+$ and $z=0^-$ be identical throughout the bonded region in Figures 2 and 3. In three-dimensional analyses, the displacement compatibility can be satisfied by constraining the nodes along and ahead of the debond front to have identical translations. Similar constraints can be used in plate element analyses. However, the degree to which the nodal rotations along and ahead of the debond front in plate element analyses should be constrained is not obvious.

Strain energy release rates for debond configurations modeled with 4-noded assumed natural coordinate strain (ANS) plate elements (Figure 6(a)) can be calculated by means of the virtual crack closure technique from the work required to close the debond from $a+\Delta$ to a. Referring to Figure 6(b), this work term can be computed from the nodal forces (F) and moments (M) at nodes i and i', and the relative displacements (u, v, w, θ_x, θ_y, θ_z)

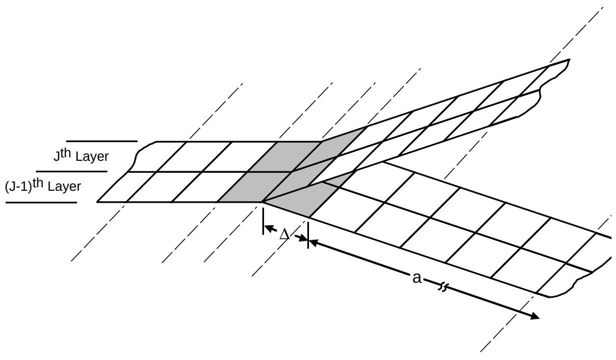

(a) Plate element modeling near the debond front

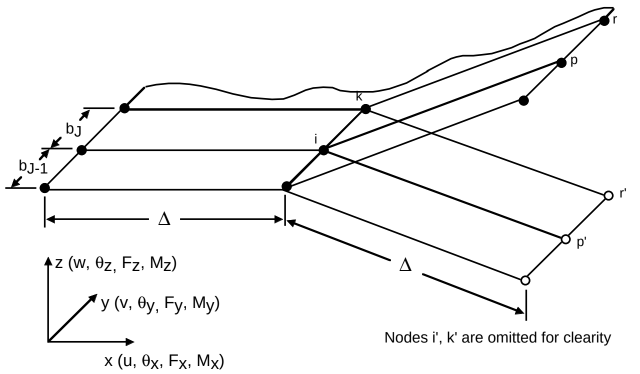

(b) Details of the model near the debond front

Figure 6 : Debond configuration modeled using 4-node plate elements.

between nodes *p* and *p'*. Note that the nodes *i'* and *k'* for the bottom plate in Figure 6 are omitted for clarity. If each of the six displacement and traction components contributes to the energy associated with debond growth, then the formulae for computing the strain energy release rate for an orthogonal and symmetric mesh of plate elements about the debond front are given by

$$
\begin{aligned}
G_I &= \frac{-1}{2\Delta b_{eq}} \begin{bmatrix} F_{x'}(w_p - w_{p'} + M_{x'}(\theta_{x_p} - \theta_{x_{p'}}) \\ +M_{y_i}(\theta_{y_p} - \theta_{y'_p}) \end{bmatrix} \\
G_{II} &= \frac{-1}{2\Delta b_{eq}} \left[F_{x_i}(u_p - u_{p'})\right] \\
G_{III} &= \frac{-1}{2\Delta b_{eq}} \left[F_{y_i}(v_p - v_{p'}) + M_{z_i}(\theta_{z_p} - \theta_{z_{p'}})\right] \\
G_{Total} &= G_I + G_{II} + G_{III}
\end{aligned}
\tag{4}
$$

where

$$b_{eq} = \frac{1}{2}\left[b_{J-1} + b_J\right]$$

with b_{J-1} and b_J being the width of the $(J\text{-}1)^{th}$ and J^{th} strips (see Figure 6) and b_{eq} being the equivalent width apportioned to node *i* [Raju, Sistla, and Krishnamurthy (1996)].

If the rotational constraints are applied to paired nodes (*e.g.*, *i* and *i'*), then the moments (M_{xi}, M_{yi} and M_{zi}) will be nonzero as in Eq. 4. Conversely, if there are no rotational constraints at and ahead of the debond front then the moments (M_{xi}, M_{yi} and M_{zi}) are identically zero as no external moment is applied at node *i* and Eq. 4 simplifies to[Wang and Raju (1996)]

$$
\begin{aligned}
G_I &= \frac{-1}{2\Delta b_{eq}} \left[F_{z_i}\left(w_p - w_p\right)\right] \\
G_{II} &= \frac{-1}{2\Delta b_{eq}} \left[F_{x_i}\left(u_p - u_p\right)\right] \\
G_{III} &= \frac{-1}{2\Delta b_{eq}} \left[F_{y_i}\left(v_p - v_p\right)\right]
\end{aligned}
\tag{5}
$$

Equations 4 and 5 correspond to “Technique-A” and “Technique-B,” respectively, in Wang, Raju, Davila, and Sleight (1993) and Wang and Raju (1996). In these references, Technique-B was shown to give accurate *G*-values when compared to *G*-values from 2D plane strain analyses. Similar equations for 9-noded ANS plate elements that account for the contribution from the midside and midface nodes were presented in Wang, Raju, and Sleight (1995).

2.3.2 Shear Deformation Assumptions

Plate elements have been developed extensively since their inception in the 1960's [Zienkiewicz and Taylor (1991); Hrabok and Hrudey (1984)]. Unlike 2D plane strain or 3D analyses, plate element-based analyses assume a particular state of shear deformation within the structure being modeled such as Kirchhoff, Mindlin and Reissner assumptions. For example, plate elements based on Kirchhoff plate theory neglect shear deformation by assuming that plane sections remain plane and normal to the element midplane while Mindlin plate elements assume independent rotations and account for shear deformation. In the present discussion, 4-noded ANS plate elements with no shear defomation and 9-noded ANS plate elements with first order shear deformation are considered. Strain energy release rates computed from analyses using each of these plate elements are compared with values from 2D plane strain analyses. The effects of shear deformation modeling on the calculation of G is discussed.

2.3.3 Continuity of Material and Section Properties

The oscillatory singularity near the front of a debonded bimaterial interface is a well known artifact of linear elastic fracture mechanics calculations [Williams (1959); Erdogan (1965); Rice and Sih (1965); Rice (1988); Comninou (1987); Hutchinson, Mear, and Rice (1987)]. The individual modes of the strain energy release rate calculated from finite element analyses do not converge with increasing mesh refinement for the interfacial debond, although the total strain energy release rate does converge rapidly with mesh refinement [Raju, Crews, and Aminpour (1988)]. This effect is readily seen in finite element analyses using 2D plane strain elements that model the cross-section or in three-dimensional configurational models [Raju, Crews, and Aminpour (1988)]. The question "would the same effect be observed when plate element modeling is used?" is a logical question that needs to be addressed.

The configuration shown in Figure 3(a) is used to examine the convergence of the components of the strain energy release rate. The effect of dissimilarities of the material and cross-sectional configuration of the skin and stiffener flange on the sensitivity of the individual modes of strain energy release rate to mesh refinement is discussed.

3 Results and Discussion

The effects of nodal constraint, shear deformation and continuity of material properties on the computed value of the strain energy release rate are presented and discussed in this section. First, the DCB configuration shown in Figure 2(a) is used to illustrate the effects of assumed shear deformation and local rotational and mid-side node translational constraint. Next, the simplified stiffener debond configuration shown in Figure 3(a) is used to determine the sensitivity of the plate element-based analyses to the slenderness ratio of the model and to the actual state of shear deformation near a debond front. Finally, the stiffener debond configuration (Figure 3(a)) is used to study the effects of continuity of material properties.

A 2D plane strain finite element code, FRANC2D [Wawrzynek and Ingraffea (1994)] and a shell finite element code, STAGS [Brogan, Rankin, Cabiness, and Loden (1996)], were used in these analyses. The FRANC2D model uses quadratic triangular and quadrilateral elements with a rosette of quarter-point (singular) triangles at the debond front. The STAGS element library includes two elements that are candidates for modeling the debond configurations shown in Figures 2 and 3: a linear Lagrangian element having no shear deformation and a quadratic Lagrangian element that includes first order shear deformations.

3.1 Nodal Constraint and Shear Deformation Assumptions

3.1.1 Nodal Constraint and Assumed Shear Deformation

A DCB configuration, as shown in Figure 2(a), with a unit applied shear load was analyzed. The material was assumed to be isotropic and homogeneous with a Young's modulus of 10.0x10^6 psi and a Poisson's ratio of 0.30.

Two-dimensional plane strain solutions were obtained using the finite element code FRANC2D for debond lengths, a, between 0.01 and 0.50 in. for three values of beam length, l. Strain energy release rates calculated in these analyses are shown in Figure 7. For the DCB configuration G_I=G_{Total}. The analyses show that the beam length, l, has negligible effect on the strain energy release rates until approximately a/h=7, a/h=14, a/h=20 for l/h=10, l/h=20, l/h=40, respectively. This corresponds to

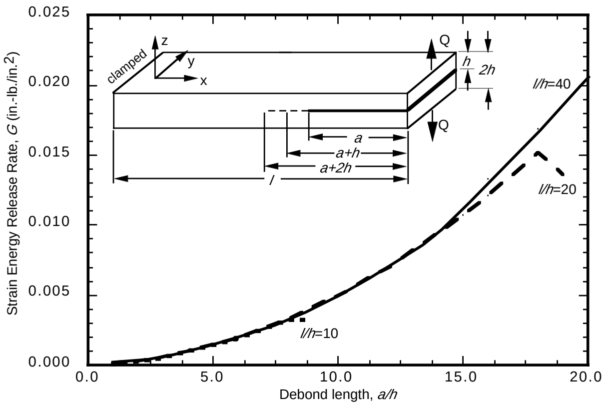

Figure 7 : Strain energy release rate for several length beams under unit load.

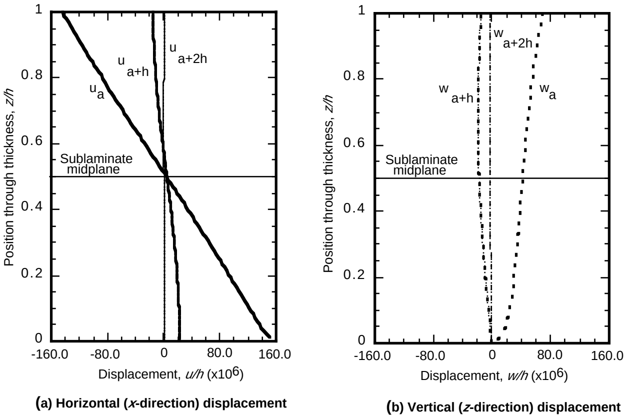

(a) Horizontal (*x*-direction) displacement

(b) Vertical (*z*-direction) displacement

Figure 8 : Displacements along three vertical planes near the debond front.

approximately *a*/*l*=0.8. Note that if the debond length is significantly shorter than the length of the beam, the strain energy release rate is only a function of the debond length, *a*, and the beam thickness, *h*.

Table 1 : Plate Element Modeling Methods (see also Figure 9)

Method	Shear Deformable Element	DOF Constrained
1	Yes	w_n=$w_{n'}$— *allnodes*
2	Yes	w_n=$w_{n'}$—*edgenodes*
3	Yes	w_n=$w_{n'}$—*allnodes* θ_{yn}=$\theta_{yn'}$—*allnodes*
4	No	w_n=$w_{n'}$—*allnodes*
5	No	w_n=$w_{n'}$—*allnodes* θ_{yn}=$\theta_{yn'}$—*allnodes*

Displacements in the *x*- and *z*-directions along vertical sections of the beam are presented in Figure 8. Three vertical sections are taken normal to the *x*-axis. The first section is taken at the debond front, the second at one plate thickness (*h*) ahead of the debond front, and the third at two plate thicknesses (2*h*) ahead of the debond front. For the first section located at the debond front, maximum displacements in the *x*-direction (thick solid line, Figure 8(a)) are larger than the maximum displacements in the *z*-direction (thick dotted line, Figure 8(b)). Here, displacements in the *x*-direction are approximately a linear function of position through the thickness. That is, the plate theory assumption that plane sections remain plane is reasonable at the debond front for this configuration. Displacements along the second vertical section at *a*+*h* in both the *x*-direction (medium solid line) and the *z*-direction (medium dashed line) are approximately 10% of the corresponding displacements along the vertical section at the debond front. The displacements along the third vertical section at *a*+2*h* in the *x*-direction (fine solid line) and *z*-direction (fine dashed line) are negligible, consistent with thin plate assumptions.

Wang, Raju, Davila, and Sleight (1993) and Wang and Raju (1996) suggested releasing the rotational degrees of freedom ahead of the debond front in plate or shell analyses of debond problems to allow deformations in the *x*-direction similar to those shown in Figure 8(a). This methodology resulted in accurate energy release rate calculations for debond problems using plate elements. In this paper, five different methods of modeling near-debond front deformations are considered and all nodes (0=*x*=*l*-*a*, *z*=0) have these constraints. For convenience in presentation, the modeling techniques will be referred to here as nodal constraint methods. These methods use two different elements, and constrain different degrees of freedom ahead of the debond front, as summarized in Table 1 and Figure 9. The ability of these methods to model near-debond front deformations (such as those shown in Figure 8) accurately has a significant effect on the accuracy of the corresponding energy release rate calculations.

Figure 10 is a plot of strain energy release rate as a function of debond length (*G* vs. *a*) using the five nodal constraint methods, as well as the baseline plane strain solution. For the range of debond lengths of 0¡*a*/*h*¡10, both

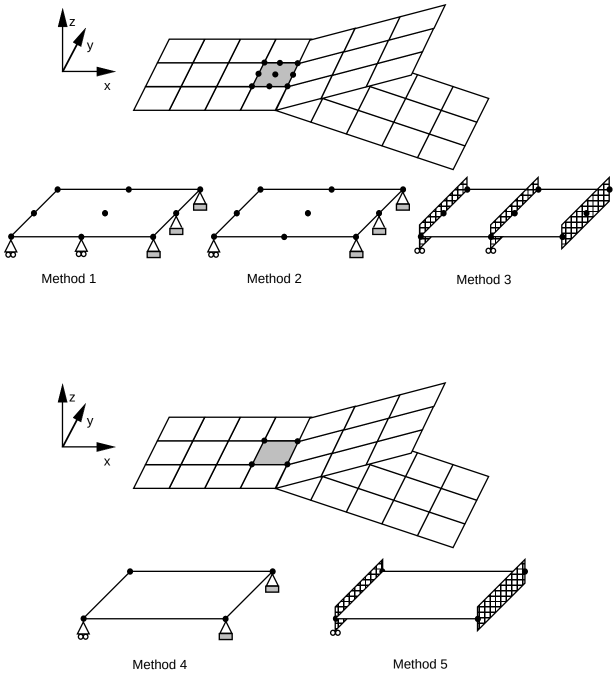

Figure 9 : Plate element modeling methods for elements ahead of debond front.

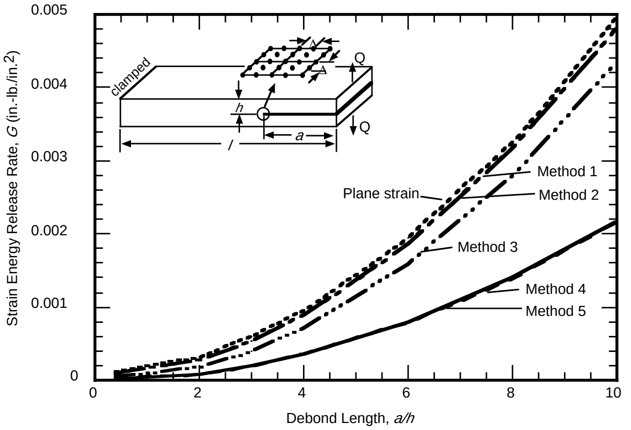

Figure 10 : Strain energy release rate for five methods and plane strain. (Q=1.0 lb./in.)

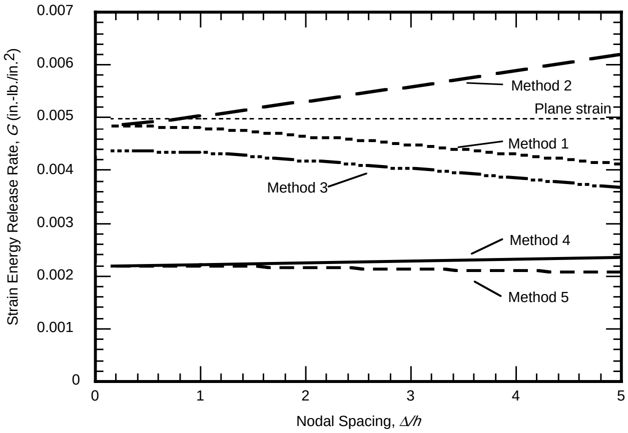

Figure 11 : Convergence of strain energy release rate. (a=0.25, h=0.025)

Method 1 and Method 2 approximate the plane strain solution well. Method 3 underpredicts G values by 5% to 10%. Method 4 and Method 5, which do not account for shear deformation, underpredict G values by as much as 50%.

Figure 11 shows the convergence characteristics of the strain energy release rate (with mesh refinement Δ/h) calculated by the nodal constraint methods for a single value of a/h. A comparison of the converged G-values, predicted with the plate element methods, to the plane strain solution illustrates the need for proper modeling of shear deformation. The deformation shown in Figure 8 is an essential aspect of the deformation field near the debond front that cannot be modeled accurately by plate elements that do not allow shear deformations. Methods 4 and 5 do not allow for shear deformation anywhere in the model, and consequently do not predict energy release rates accurately. Method 3 has rotations restrained to be zero at and ahead of the debond front, but allows for shear deformations behind the debond front. As a result, the model is overly stiff, but predicts energy release rates much closer to the plane strain values than are predicted by Methods 4 and 5.

Both Methods 1 and 2 allow rotations due to shear deformation ahead of and behind the debond front. The converged values of energy release rate for both of these methods approach the same value and are within three percent of the plane strain value. However, Method 1 converges from below while Method 2 converges from above. The element midside nodes ahead of the debond front in Method 1 (see Figure 9) are restrained against vertical displacements, whereas the same nodes in models corresponding to Method 2 are allowed to displace freely. Since Method 1 requires that each element ahead of the debond front has vertical nodal translations restrained, there can be no vertical displacement at any point in the element. Conversely, Method 2 relaxes the constraint by requiring that only the edge nodes of each element ahead of the debond front have vertical nodal translations restrained as shown in Figure 9. For any degree of mesh refinement, Method 2 allows two types of displacement to occur ahead of the debond front: translations and rotations due to both bending and shear. Thus, Method 2 tends to be overly compliant. As the mesh refinement increases, the distance between restrained end nodes of each element decreases and bending deformation reduces to zero. The converged state of this method predicts the proper shear-dominated behavior. In contrast, Method 1 has the midside and midface nodes restrained in the vertical direction. This constraint disallows the bending deformation shown in Figure 8, causing shear to be the dominant mode of deformation ahead of the debond front for any degree of mesh refinement using this method. Since Method 1 converges somewhat more rapidly than Method 2, it is considered to be the preferred method for this type of modeling and will be used for the remainder of the analyses in this paper.

3.1.2 Validity of Plate Assumptions

In this section, the effect of assumptions associated with using Mindlin plate elements [Zienkiewicz and Taylor (1991)] for calculation of the strain energy release rates are discussed. Geometrically linear analyses with a unit load, Q, are considered as shown in Figure 3(a). For the purposes of illustration, a skin-stiffener debond configuration is assumed. The skin and stiffener flange are assumed to be constructed of unidirectional graphite/epoxy plies with properties [Wang, Raju, Davila, and Sleight (1993); Wang and Raju (1996)]

E_{11}=19.5x10^6 psi E_{22}= E_{33}=1.48x10^6 psi
μ_{12}= μ_{13}=0.80x10^6 psi μ_{23}=0.497x10^6 psi
υ_{12}=υ_{13}=0.30 υ_{23}=0.49

where E_{ii}, μ_{ij}, υ_{ij} (i,j=1,2,3) are the Young's moduli, shear moduli, and Poisson's ratios, respectively. The subscripts 1,2,3 represent the fiber and two transverse directions, respectively.

Figure 12(a) shows a comparison between the plate ele-

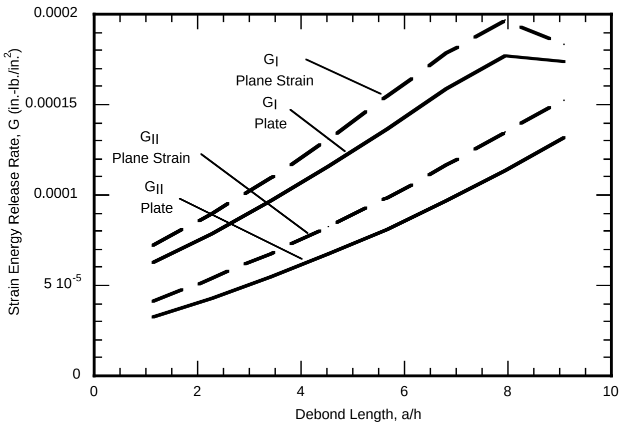

(a) Debond configurations with thickness, ($l/2h$)=9.09

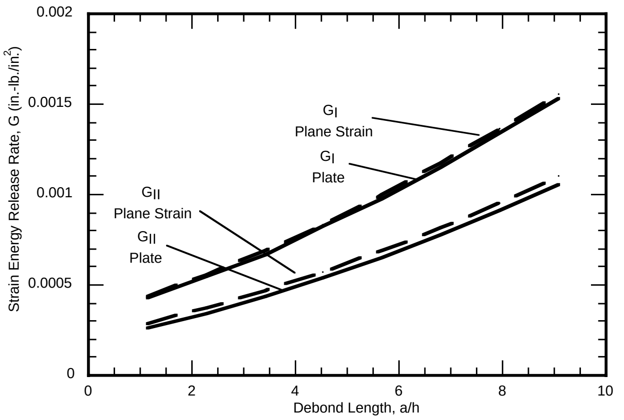

(b) Debond configurations with thickness, ($l/2h$)=18.2

Figure 12 : Comparison of shell and plane strain analysis.

ment and plane strain element-based techniques for the configuration shown in Figure 3. The configuration has a ratio of overall length to total thickness of *(l/2h)*=9.09. As seen in the figure, the plate element-based technique predicts values of G_I and G_{II} that are consistently less than the plane strain values. The difference between the two analyses is a weak function of the debond length with approximately 27 and 14 percent difference for G_I and G_{II}, respectively, at values of *a/h*=1.14 and 16 and 6 percent difference for G_I and G_{II}, respectively, at values of *a/h*=9.09.

Figure 12(b) shows a similar comparison between plate and plane strain values, but for a ratio of overall length to total thickness of *l/2h*=18.2. As seen in this figure, the plate element-based technique predicts values of G_I and G_{II} that are only slightly less than the plane strain values. The difference between the two analyses is again a weak function of the debond length with approximately 9 and 1 percent difference for G_I and G_{II}, respectively, at values of *a/h*=1.14 and 5 and 1 percent difference for G_I and G_{II}, respectively, at values of *a/h*=9.09. Close examination of the curves of axial displacement along a vertical plane at the debond front shown in Figure 13 reveals that the plate element assumption of plane sections remaining plane is more accurate for the configuration with the larger slenderness ratio. Thus, a comparison of the results obtained for these two configurations and an examination of the deformations shown in Figure 13 indicates that the validity of the plate element-based analyses using the STAGS 480 shear deformable plate/shell elements improves with increasing ratio of overall model length to thickness and that the accuracy is a weak function of debond length.

3.2 Continuity

This section addresses plate element modeling of skin-stiffener debond configurations where either extension-bending coupling is present or the stiffnesses on either side of the plane of the debond is discontinuous. In elastic continuum analyses, the phenomenon that results from mathematical modeling of debonds at bimaterial interfaces and the resulting discontinuity of the elastic modulus is the well known oscillatory singularity [Williams (1959); Erdogan (1965); Rice and Sih (1965); Rice (1988); Comninou (1987); Hutchinson, Mear, and Rice (1987); Raju and Dattaguru (1995); Chow and Atluri (1995)]. The reason for examining these configurations is to study the effects of material and geometric

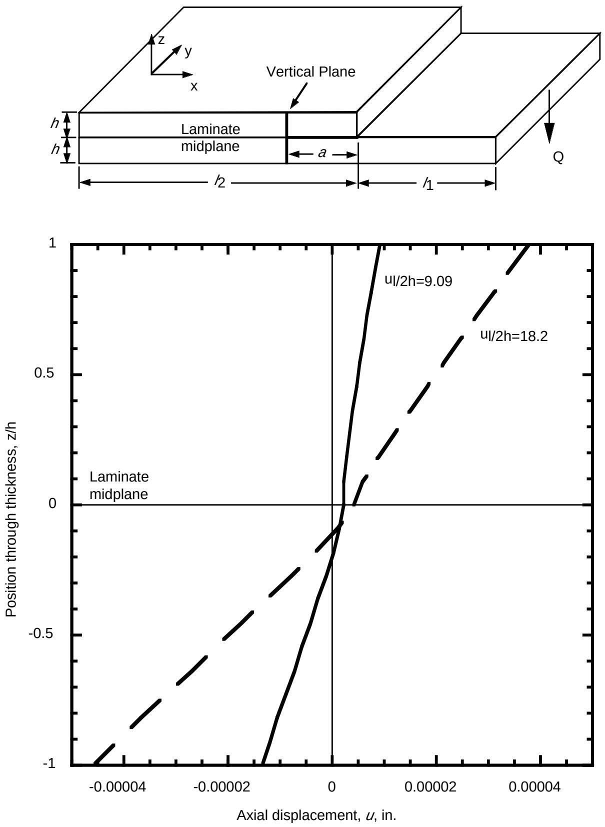

Figure 13 : Displacement along a vertical plane at the crack tip of the mixed mode debond configuration.

section property continuity on the convergence of individual modes of the strain energy release rates with decreasing element size for configurations modeled with plate elements.

The general configuration that will be used to illustrate the effect of material and stiffness continuity on the convergence of individual modes of the strain energy release rate is shown in Figure 3. The configurational parameters used here are l_1 = 2.0 in., l_2 = 2.0 in. and a = 1.0 in. Again, a unit shear load is applied. Unidirectional lamina properties and the details of the skin and stiffener flange thicknesses and layups are given in Table 2 which identifies five basic configurations. Cylindrical bending boundary conditions were applied to the model as shown in Figure 3(a). In the analyses that follow, the shear deformable quadratic element with prescribed zero z-direction translations at all nodes, corresponding to Method 1 in the previous section, is used. Strain energy release rates are computed using Eq. 5.

Figures 14-18 show the change in the computed values of mode-I (G_I), mode-II (G_{II}), and total (G_{Total}) strain energy release rates as a function of element size. Configuration 1 has the skin and flange with the same thickness and layup, *i.e.* with identical extensional, shear and bending stiffnesses. In Figure 14, both the total and the individual modes of strain energy release rate for Configuration 1 converge for even very large element sizes approaching 10% of the length (l_1+l_2 in Figure 3(a)) because there is no oscillatory singularity present in this configuration.

Figures 15-18 show the computed values of G_I, G_{II} and G_{Total} as a function of element size for Configurations 2-5, respectively. As seen in the figures, the total strain energy release rate converges even when large element sizes are considered. However, over the range of element sizes considered, the individual modes do not converge regardless of element size for each of these cases. This is due to the oscillatory nature of the singularity arising from the material and stiffness mismatch.

Configuration 2, shown in Figure 15, has a skin and flange with the same thickness, but with an unsymmetric layup in the flange. Thus, the flange has different extension, shear and bending stiffnesses than the skin. In addition, the flange exhibits extension-bending coupling [Jones (1975)]. The individual effects of extension-bending coupling and differing skin and stiffener stiff-

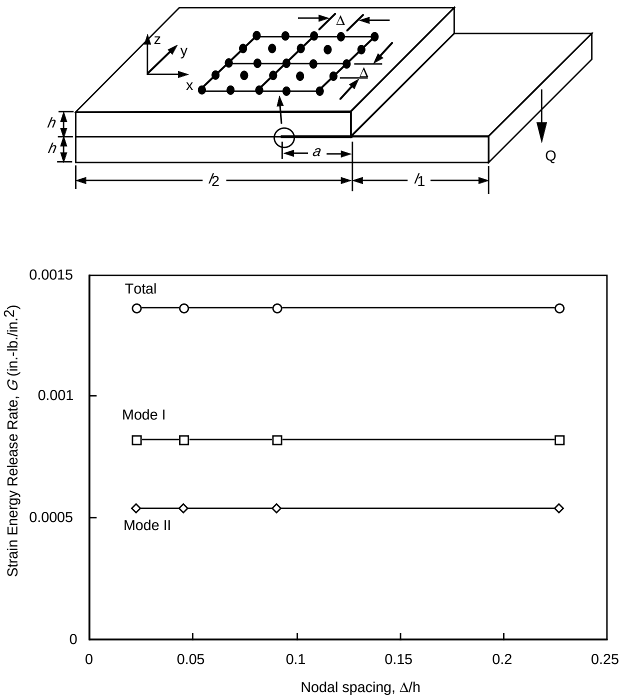

Figure 14 : Strain energy release rate for debond configuration with similar flange and skin. (Configuration 1)

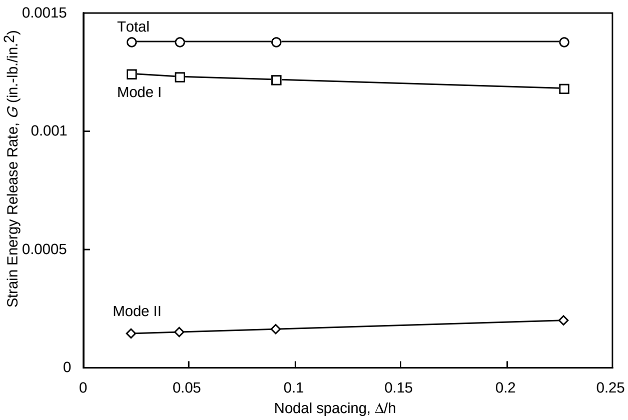

Figure 15 : Strain energy release rate for debond configuration with unsymmetric flange. (Configuration 2)

Table 2 : Skin-Flange Configurations

Configuration	Flange Thickness (in)	Flange Layup	Skin Thickness (in)	Skin Layup	Plies at Interface
1	0.11	$[0]_{20}$	0.11	$[0]_{20}$	0/0
2	0.11	$[0_{10}/90_{10}]$	0.11	$[0]_{20}$	90/0
3	0.11	$[0_{10}/90_{10}]$	0.11	$[0_{10}/90_{10}]$	90/0
4	0.11	$[0_5/90_{10}/0_5]$	0.11	$[0]_{20}$	0/0
5	0.055	$[0]_{10}$	0.11	$[0]_{20}$	0/0

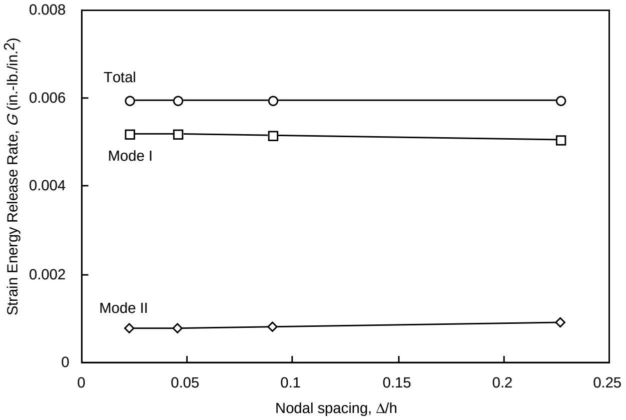

Figure 16 : Strain energy release rate for debond configuration with unsymmetric skin and flange. (Configuration 3)

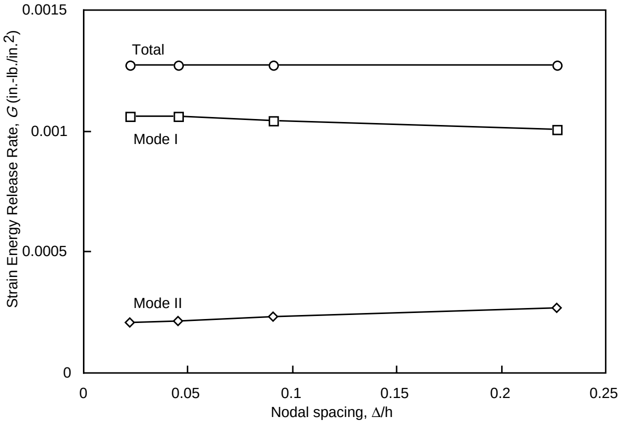

Figure 17 : Strain energy release rate for debond configuration with skin and flange with different stiffness. (Configuration 4)

nesses can be examined by considering Configurations 3 and 4, respectively. Figure 16 shows the results for Configuration 3 where the skin and flange are both unsymmetric. Although they both have identical extension, shear and bending stiffnesses, the modes fail to converge throughout the range of element sizes considered. Thus, extension-bending coupling alone is sufficient to inhibit convergence of the individual modes over this broad range of element sizes. Figure 17 shows the strain energy release rate for Configuration 4, where the skin and flange have the same thickness. Although the flange is symmetric and has no extension-bending coupling, it has different extension, shear and bending stiffnesses than the skin. Thus, different stiffnesses for the skin and flange alone is sufficient to inhibit convergence of the individual modes. Finally, Figure 18 shows the results for Configuration 5 where the skin and flange have the same layup, but different thicknesses. This configuration is similar to Configuration 4 in that the skin and flange have different stiffness with no coupling. Again, the individual modes fail to converge over the range of element sizes that were considered. In all cases the total strain energy release rate converged rapidly.

4 Concluding Remarks

The effects of several critical assumptions and parameters on the computation of strain energy release rates for delamination and debond configurations modeled with plate elements were studied. The issues studied were: constraint of translational degrees of freedom, rotational degrees of freedom or both in the neighborhood of the debond front; shear deformation assumptions; and continuity of material properties and section stiffness in the vicinity of the debond.

The analyses suggest that properly accounting for the effects of shear deformation and assumed compatibility are critical when computing the strain energy release rates with the virtual crack closure technique (VCCT) applied to plate elements. Five nodal constraint methods for implementing plate elements in these calculations were compared. The method in which shear deformation was

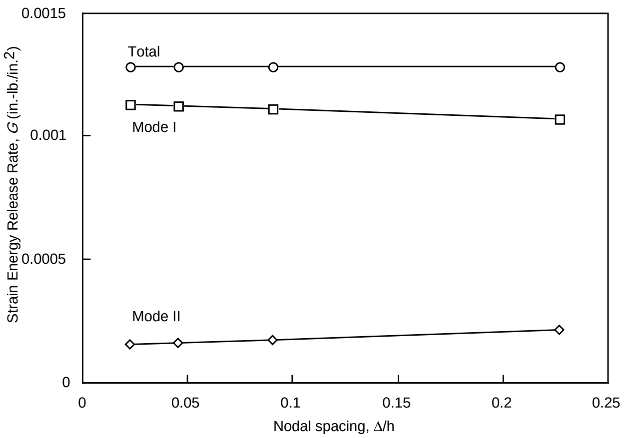

Figure 18 : Strain energy release rate for debond configuration with flange with half of the skin thickness. (Configuration 5)

included and vertical nodal translations were restrained at all nodes ahead of the debond front was determined to be the preferable method because it most rapidly converges to the plane strain solutions. However, the limitation of using plate elements for accurately computing strain energy release rates for configurations with small slenderness ratios is evident even when first order shear deformations are considered. Differences in computed G_I-values from the plate and the plane strain solutions of as much as 27 percent for (*l/2h)*=9.09 were observed.

The results of the simulations of the debond configurations with discontinuous section properties suggest that some or all of the characteristics of the classical bimaterial interface problem can be present when modeling with this plate element-based technique. In the plate element models, the section properties depend on both material and geometric properties. When the section properties above and below the debonded plane are discontinuous, the total strain energy release rate converges, but the modes do not converge or converge very slowly. Conversely, when the section properties are continuous, both the total strain energy release rate and the individual modes converge rapidly.

References

Atluri, S.N. (1997)*: Structural Integrity and Durability*, Tech Science Press, Forsyth, GA, 865 pages.

Broek, D. (1987): *Elementary Engineering Fracture Mechanics*, 4th Edition, Martinus Nijhoff, Boston, MA.

Brogan, F.A.; Rankin, C.C.; Cabiness, H.D.; Loden, W.A. (1996): *STAGS User Manual*, Lockheed Martin Missiles and Space Co.

Chow, W.-T., and Atluri, S.N. (1995): ”Finite Element Calculation of Stress-Intensity Factors for Interfacial Crack Using Virtual Crack Closure Integral,” *Computational Mechanics*, Vol. 16, pp. 1-9.

Chow, W.T.; Atluri, S.N. (1996): ”Prediction of Post-Buckling Strength of Stiffened Laminated Composite Panels Based on the Criterion of Mixed-Mode Stress Intensity Factors,” *Computational Mechanics*, Vol. 18, No. 3, pp. 215-224.

Cohen, D.; Hyer, M.W. (1988): “Influence of Geometric Nonlinearities on Skin-Stiffener Interface Stresses,” *29th AIAA/ASME/ASCE/AHS Structures, Structural Dynamics and Materials Conference*, AIAA Paper 88-2217-CP.

Comninou, M. (1987): “The Interface Crack,” *Journal of Applied Mechanics*, Vol. 54, 1987, pp. 828-832.

Erdogan, F. (1965): “Stress Distribution in Bonded Dissimilar Materials with Cracks,” *Journal of Applied Mechanics*, Vol. 32, pp. 403-410.

Hrabok, M.M.; Hrudey, T.M. (1984): “A Review and Catalog of Plate Bending Finite Elements,” *Computers and Structures*, Vol. 19, No. 3, pp. 479-495.

Hutchinson, J.W.; Mear, M.E.; Rice, J.R. (1987): “Crack Paralleling an Interface Between Dissimilar Materials,” *Journal of Applied Mechanics*, Vol. 54, pp. 828-832.

Hyer, M.W.; Cohen, D. (1987): “Calculation of Stresses and Forces Between the Skin and Stiffener in Composite Panels,” *28th AIAA/ASME/ASCE/AHS Structures, Structural Dynamics and Materials Conference*, AIAA Paper 87-0731-CP.

Irwin, G.R. (1958): “Fracture,” *In Handbuch der Physik*, Vol. 6, p. 551.

Jones, R.M. (1975): *Mechanics of Composite Materials*, Hemisphere Publishing Corporation, New York.

Naganarayana, B. P., and Atluri, S.N. (1995): ”Energy-Release-Rate Evaluation for Delamination Growth Prediction in a Multi-Plate Medal of a Composite Laminate,” *Computational Mechanics*, Vol. 15, pps. 443-459.

O’Brien, T.K. (1982): “Characterization of Delamination Onset and Growth in a Composite Laminate," *Damage in Composite Materials*, *ASTM STP 775*, pp. 140-167.

Raju, I.S. (1987): "Calculation of Strain-Energy Release Rates with Higher Order and Singular Finite Elements," *Engineering Fracture Mechanics*, Vol. 28, No. 3, pp. 251-274.

Raju, I.S.; Crews, Jr., J.H.; Aminpour, M.A. (1988): "Convergence of Strain Energy Release Rate Components for Edge-Delaminated Composite Laminates," *Engineering Fracture Mechanics*, Vol. 30, No. 3, pp. 383-396.

Raju, I.S.; Dattaguru, B. (1995): "Review of Methods for Calculating Fracture Parameters for Interface Crack Problems," *Computational Mechanics 1995: Proceedings of the International Conference on Computational Engineering Science*, S.N. Atluri, G. Yagawa and T.A. Cruise, eds., pp. 2020-2026.

Raju, I.S.; Sistla, R.; Krishnamurthy, T. (1996): "Fracture Mechanics Analyses for Skin-Stiffener Debonding," *Engineering Fracture Mechanics*, Vol. 54, No. 3, pp. 371-385.

Rice, J.R. (1988): "Elastic Fracture Mechanics Concepts for Interface Cracks," *Journal of Applied Mechanics*, Vol. 55, pp. 98-103.

Rice, J.R.; Sih, G.C. (1965): "Plane Problems of Cracks in Dissimilar Media," *Journal of Applied Mechanics*, Vol. 32, pp. 418-423.

Rybicki, E.F.; Kanninen, M.F. (1977): "A Finite Element Calculation of Stress Intensity Factors by a Modified Crack Closure Integral," *Engineering Fracture Mechanics*, Vol. 9, pp.931-938.

Shiah, Y. C.; Tan, C. L. (2000): "Fracture Mechanics Analysis in 2-D Anisotropic Thermoelasticity Using BEM". *CMES*: *Computer Modeling in Engineering & Sciences*, Vol. 1, No. 3, pp. 91-99.

Wang, A.S.D.; Crossman, F.W. (1980): "Initiation and Growth of Transverse Cracks and Edge Delamination in Composite Laminates, Part 1: An energy method," *Journal of Composite Materials*, Vol. 14, pp. 71-87.

Wang, J.T.; Raju, I.S. (1996): "Strain Energy Release Rate Formulae for Skin-Stiffener Debond Modeled with Plate Elements," *Engineering Fracture Mechanics*, Vol. 54, No. 2, pp. 211-228.

Wang, J.T.; Raju, I.S.; Davila, C.G.; Sleight, D.W. (1993): "Computation of Strain Energy Release Rates for Skin-Stiffener Debonds Modeled with Plate Elements," 34th *AIAA/ASME/ASCE/AHS Structures, Structural Dynamics and Materials Conference*, AIAA Paper 93-1501-CP, pp. 1680-1692.

Wang, J.T.; Raju, I.S.; Sleight, D.W. (1995): "Composite Skin Stiffener Debond Analyses Using Fracture Mechanics Approach with Shell Elements," *Composites Engineering*, Vol. 5, No. 2, 1995, pp. 277-296.

Wang, J.T.S.; Biggers, S.B. (1984): "Skin/Stiffener Interface Stresses in Composite Stiffened Panels," *NASA CR 172261*.

Wawrzynek, P.; Ingraffea, A. (1994): *FRANC2D: A Two-Dimensional Crack Propagation Simulator*, NASA CR-4572.

Whitcomb, J.D. (1988): "Instability-Related Delamination Growth of Embedded and Edge Delaminations," *NASA TM 100655*.

Williams, M.L. (1959): "The Stresses Around a Fault or Crack in Dissimilar Media," *Bull. Seismol. Soc. Am.*, Vol. 49, pp. 199-204.

Zienkiewicz, O.C.; Taylor, R.L. (1991): *The Finite Element Method*, 4th Edition, McGraw-Hill Book Company Europe, Berkshire.